An examination of convective moistening of the lower stratosphere using satellite data

Ying Sun[1] and Yi Huang[1]

[1]Department of Atmospheric and Oceanic Sciences, McGill University, Montreal, Quebec, Canada

Abstract In this paper, we use satellite data to test the hypothesis that deep convection moistens the lower stratosphere. Water vapor measurements from Earth Observing System-Microwave Limb Sounder and Atmospheric Chemistry Experiment-Fourier Transform Spectrometer over North America are binned according to the International Satellite Cloud Climatology Project deep convection indices. The results show that in the North American region (50–112°W, 10–50°N) the convection-impacted samples are significantly moister than the nonimpact samples in the lowermost stratospheric layer right above the tropopause, and a drier tendency is also noticed right above this moistened layer. Trajectory modeling is used to aid the identification of deep convection-impacted water vapor samples. However, we find that a substantial fraction of high-concentration (>8 ppmv) samples at 100 hPa cannot be attributed to nearby deep convections.

1. Introduction

Despite its scarcity (~3–5 ppmv), stratospheric water vapor (SWV) is a climatically important atmospheric constituent due to its significant radiative and chemical impacts [*Forster and Shine*, 1999; *Solomon et al.*, 2010; *Anderson et al.*, 2012]. Recent studies have particularly addressed whether and how SWV variation may be coupled with tropospheric and surface temperatures and constitute a radiative feedback that affects climate sensitivity. *Huang* [2013] shows that the overall stratospheric radiative effect in coupled general circulation models may amount to $0.3\,W\,m^{-2}\,K^{-1}$; *Dessler et al.* [2013] postulates that SWV alone may result in a feedback of this magnitude and especially highlight the effect of water vapor in the lower stratosphere.

Assessment of the climatic impact of SWV is impeded by the lack of understanding of processes that control its distribution and variation. An important process, transport by the overturning Brewer-Dobson Circulation, has been long recognized [*Brewer*, 1949]. However, it is uncertain how factors such as temperature in the tropical tropopause layer, strength of circulation, and vertical and horizontal mixing are weighted and interactively determine SWV distribution and variation [*Fueglistaler et al.*, 2014]. Some long-term trends in the site record (e.g., the balloon measurements taken in Boulder, Colorado) cannot be fully explained by the known factors, and the abrupt decrease in global mean SWV after the year 2000 remains a mystery [*Hartmann et al.*, 2013]. On a relevant note, it is important to bear in mind that accurately measuring water vapor at low concentrations and monitoring its global, climatic variations remain a challenge. The intercalibration issue between different in situ instruments has been a long-standing issue [e.g., *Weinstock et al.*, 2009]. There are also considerable systematic biases between different satellite data sets [*Hegglin et al.*, 2013]. Moreover, regional near-surface measurements and satellite data differ in terms of spatial representativeness, which potentially lead to opposite estimates of water vapor trend [*Hegglin et al.*, 2014].

Besides methane oxidation that mostly affects the upper stratospheric water vapor budget, another process that affects SWV is overshooting deep convection, which penetrates the tropopause and is capable of directly injecting water vapor into the lower stratosphere. This moistening effect is evident from field measurements, e.g., those of *Anderson et al.* [2012]. It has been postulated that this may form an effective troposphere-stratosphere water vapor transport mechanism [*Fu et al.*, 2006]. *Hanisco et al.* [2007] show isotopic evidence that summertime extratropical convective storms make a considerable contribution to stratospheric water vapor over the North American continent. Although global SWV climatology from satellite observations, such as Atmospheric Chemistry Experiment-Fourier Transform Spectrometer (ACE-FTS) [*Randel et al.*, 2012] and Aura Microwave Limb Sounder (MLS) [*Schwartz et al.*, 2013], show prominent seasonal SWV anomalies in the Asian and North American monsoon regions that seem to corroborate the

account of convective impact, SWV and deep convection maxima are not spatially overlapped in both monsoon regions and the HDO signatures that are indicative of deep convection intriguingly differ between the two monsoon regions [*Randel et al.*, 2012]. There is also noticeable discrepancy between the in situ SWV measurements and the collocated MLS samples during moistening events [*Schwartz et al.*, 2013]. In short, it is unclear to what extent convection may affect SWV at regional or global scales. Satellite analysis of such effect is particularly lacking.

In this paper, we examine the relationship between SWV and deep convection (DC) by diagnosing satellite data sets, with a focus on the North American region (50–112°W, 10–50°N). Specifically, we (1) investigate the covariations of SWV and DC, (2) examine whether SWV concentrations differ with respect to DC occurrence, and (3) examine whether the high-concentration SWV samples can be explained by DC. The data sets and model used in our analysis will be described in the following section. Then the SWV-DC relationship diagnosed from the different perspectives will be presented. Discussion of the results and some conclusions will be given at the end.

2. Data and Methodology

2.1. Water Vapor Data

We mainly use data from Earth Observing System-Microwave Limb Sounder (MLS) aboard the NASA Aura satellite for describing SWV distribution and variation. Aura was launched in July 2004. It is a Sun-synchronous polar-orbiting satellite with a 1:45 P.M. equator crossing time and a period of about 100 min (i.e., circling the Earth about 14.5 times each day). The MLS retrieves temperature, water vapor, and other trace gases by measuring the thermal emission of the atmosphere at multiple microwave bands (the 190 GHz band is used for water vapor retrieval). Due to the 25 s measurement rate, the along-track spacing of samples is about 1.5° or about 165 km. Water vapor retrieval is given at fixed pressure levels, from 316 hPa upward. The vertical resolution of water vapor data is about 3 km in the upper troposphere and lower stratosphere (UTLS) region that we are most interested in. Details of retrieval algorithm are given by *Livesey et al.* [2006]. The uncertainty range of MLS SWV data is about 20% between 316 hPa and 147 hPa and 10% at 100 hPa and stratosphere [*Read et al.*, 2007; *Jiang et al.*, 2010]. The level 2 retrieval data (version 3.3) taken during the period from January 2005 to June 2008 are used in this study. As we are especially interested in the high-concentration samples, we have conducted a strict quality control process recommended by the MLS science team [*Livesey et al.*, 2011]. Specifically, we have used these flags to screen the data: (1) only values located within 316–0.002 hPa are used, (2) data points for which L2gpPrecision is set negative are removed, (3) profiles for which "status" is an odd number are removed, (4) profiles whose "quality" field is less than 1.3 or "convergence" field is greater than 2.0 are removed, (5) profiles having high or low cloud status flag bits set are removed, and (6) profiles of which concentration is lower than the minimum measurable water vapor concentration at a specific level are removed.

In addition, we analyze version 3.0 SWV data from ACE-FTS, which is aboard a Canadian satellite, SCISAT, launched in August 2003 [*Bernath et al.*, 2005]. ACE-FTS uses solar occultation in the spectral range of 750–4400 cm^{-1} to retrieve water vapor concentration. ACE-FTS has similar sampling footprint to that of MLS: about 300 km in the horizontal and 3–4 km in the vertical. One advantage of this instrument is that the isotopic composition of some species such as HDO can be made available. However, due to limitations of the solar occultation technique, ACE-FTS water vapor data are limited in spatial and temporal coverage and are much less abundant than MLS data. Hence, this data set is used here mainly for verification of some analysis results. We will focus on the MLS results in the following sections.

2.2. Deep Convection Data

Here we use deep convective tracking data from the International Satellite Cloud Climatology Project (ISCCP-CT) [*Machado and Rossow*, 1993] for the period (January 2005 to June 2008) that overlaps with MLS and ACE-FTS data sets. ISCCP data come from five geostationary satellites. We will use GOES-EAST data for the domain 50–112°W, 10–50°N because we are most interested in the North American region.

The ISCCP-CT data set was developed to identify deep convection by analyzing image pixels of the ISCCP pixel-level data (DX) data set [*Rossow et al.*, 1996]. Pixels that have brightness temperatures less than 245 K are
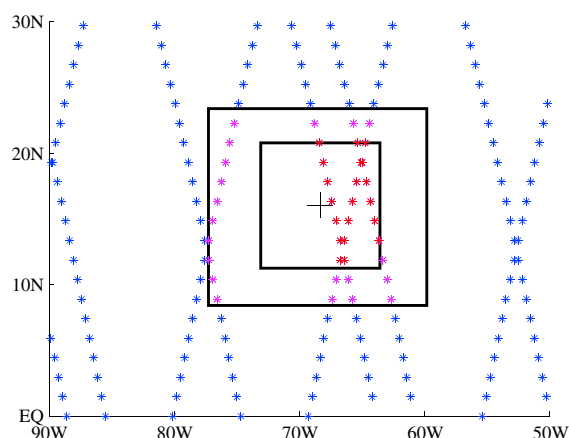
Figure 1. An example illustrating how SWV data are categorized. The black cross represents the average center of one CS family, which happened in October 2007. The two black boxes drawn from the CS size information are used for selecting storm and nonstorm samples, respectively (see details in the text). Storm samples (within the inner box) are dotted in red, nonstorm samples (outside the outer box) are in blue, and uncertain samples (in-between the two boxes) are in pink.

defined as convective system (CS), and those that have brightness temperatures less than 220 K are referred to as convective clusters (CC). Deep convective clouds range from 90 km to 350 km in size. Information including time, center position (latitude and longitude), radius, and family number of each CS are provided at 3 h time intervals and 30 km spatial intervals. Consecutive images are used to observe movement of each CS; the position and size of the CS are recorded. The same convective system detected at different time is given the same family number [*Machado et al.*, 1998].

Here we identify DC by comparing the lowest brightness temperature (LBT) recorded in the ISCCP data set to a threshold temperature. Different threshold temperatures have been used in previous works for such purpose [e.g., *Zipser et al.*, 2006; *Kubar et al.*, 2007; *Yuan and Li*, 2009; *Bedka et al.*, 2010; *Takahashi and Luo*, 2014]. We have tested different values ranging from 195 K to 245 K at 5 K interval. The results presented below are based on a threshold value of 195 K, to ensure that the DC cases selected are overshooting cases of interest. We will discuss possible impacts of this choice wherever necessary in the rest of the paper.

Based on the information provided by ISCCP-CT data, we divide MLS data into three groups: storm, nonstorm, and uncertain. Two latitude-longitude boxes are drawn here for categorizing the data. Both boxes are centered at the average center position (longitude and latitude) of each CS family within which a DC is identified. The size of the smaller box is given by the average radius of the family during its lifetime. The size of the larger box is the area covered by all CSs belonging to the family. MLS data samples falling into the smaller box are identified as "storm" samples, data outside the larger box as "nonstorm" samples, and the ones in-between as "uncertain" samples. The time window used for the storm search is set as the life period of the CS family, and the time is increased by 3 h on both ends for nonstorm search. Figure 1 illustrates an example in October 2007 of the data categorization.

2.3. Trajectory Model

The Hybrid Single-Particle Lagrangian Integrated Trajectory (HYSPLIT), version 4, is used here. This model was developed by NOAA Air Resources Laboratory [*Draxler and Hess*, 1998] and has been widely used to study aerosol transport and water vapor distribution [e.g., *Strong et al.*, 2007]. We use this model to analyze the back trajectory (historical locations) of high SWV concentration samples.

Samples are tracked on isentropic surfaces [*Newman et al.*, 2001]. A parcel at each position is traced back up to 10 days, and deep convections near the parcel locations are searched according to the same criterion used for finding storm samples above. Once a DC is encountered along the back trajectory or the trajectory extends outside the study domain (50–112°W), we will stop the tracking. To assess the uncertainty brought by the wind data, two reanalyses, National Centers for Environmental Prediction/National Center for Atmospheric Research (NCEP/NCAR) reanalysis 1 and Eta Data Assimilation System, are used here. The NCEP/NCAR reanalysis 1 provide 4 times daily data at 2.5°×2.5° horizontal resolution since 1948. The data are presented at 17 fixed pressure levels. Details can be found in *Kalnay et al.* [2006]. The Eta Data Assimilation System (EDAS) data set, which covers the U.S. region, is on a 185×129 Lambert Conformal grid with 40 km horizontal resolution and is available at 26 fixed pressure levels ranging from 1000 hPa to 50 hPa at 3 h intervals. More information is provided at https://ready.arl.noaa.gov/edas40.php. This data set covers 60–140°W North American region, so the longitude coverage in the tropics is lower. We only use the EDAS data set to calculate trajectories for samples located in the 30–50°N band because of less overlap with the study domain in the low latitudes.
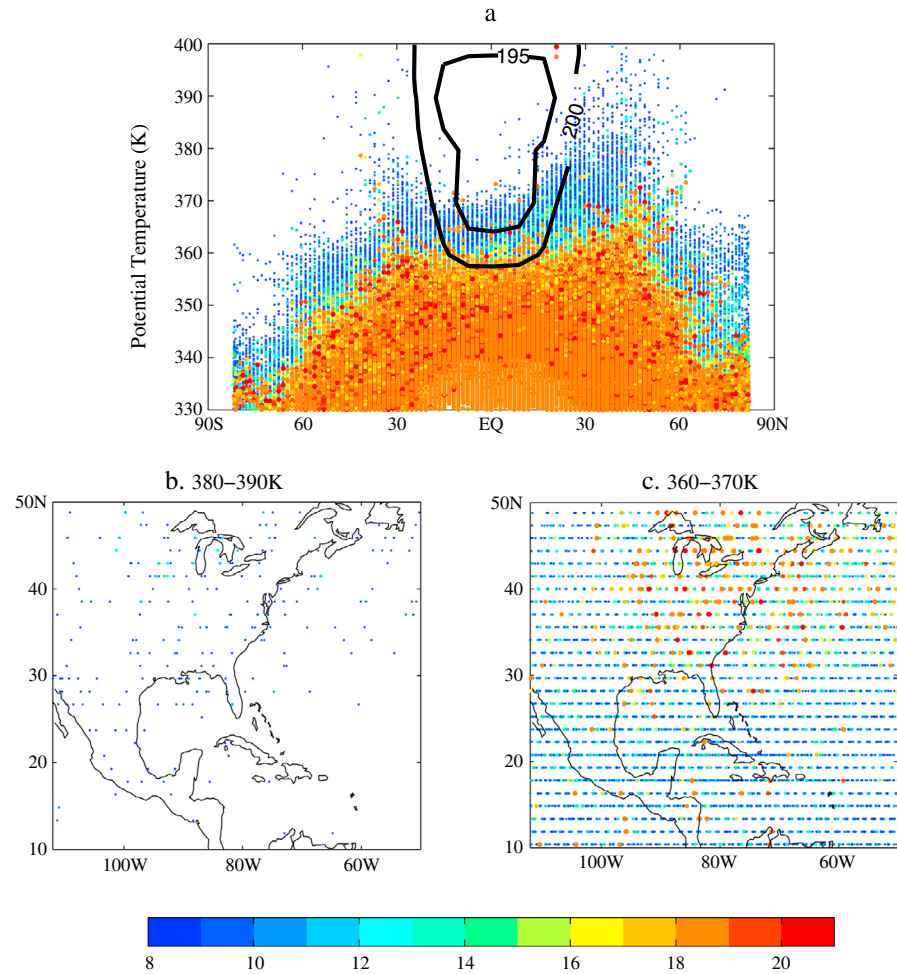
Figure 2. (a) MLS water vapor samples presented on the potential temperature-latitude cross section. The contour lines denote the absolute temperatures from MLS temperature profile. (b) MLS samples falling into the layer with potential temperature ranging from 380 to 390 K. (c) MLS samples falling into the layer with potential temperature ranging from 360 to 370 K. Unit of water vapor sample is parts per million by volume.

2.4. Auxiliary Data

In addition to the above data sets, ERA-Interim data set [*Dee et al.*, 2011] is used to provide temperature profiles for calculating the environmental tropopause position defined by the *World Meteorological Organization* [1957] criterion.

3. Results

3.1. Covariations of SWV and DC

There are a total of 169,426 MLS profiles falling into the study domain (50–112°W, 10–50°N) during the period of January 2005 to June 2008, which are used in this paper. Figure 2a illustrates the zonal distribution of the MLS data at various levels within GOES-EAST view (50–112°W) during the same period. Only samples with water vapor concentration greater than 8 ppmv are shown here. Data are presented on the latitude-potential temperature cross section. The potential temperature (θ) is calculated as $\theta = T \left(\frac{P_0}{P}\right)^{R/c_P}$, where $R/c_P = 0.286$, $P_0 = 1000$ hPa, and T and P are temperature and pressure observed at the same level as the SWV data. It is clear from the figure that a number of moist samples lie above the climatological tropopause (380 K in the tropics and 330 K/380 K (winter/summer) in the midlatitudes). These are the cases potentially related to DC. To have an overview of the distribution of high water vapor concentrations, geographic locations of samples at 360–370 K and 380–390 K are shown in Figure 2. At 360–370 K in the North American region most
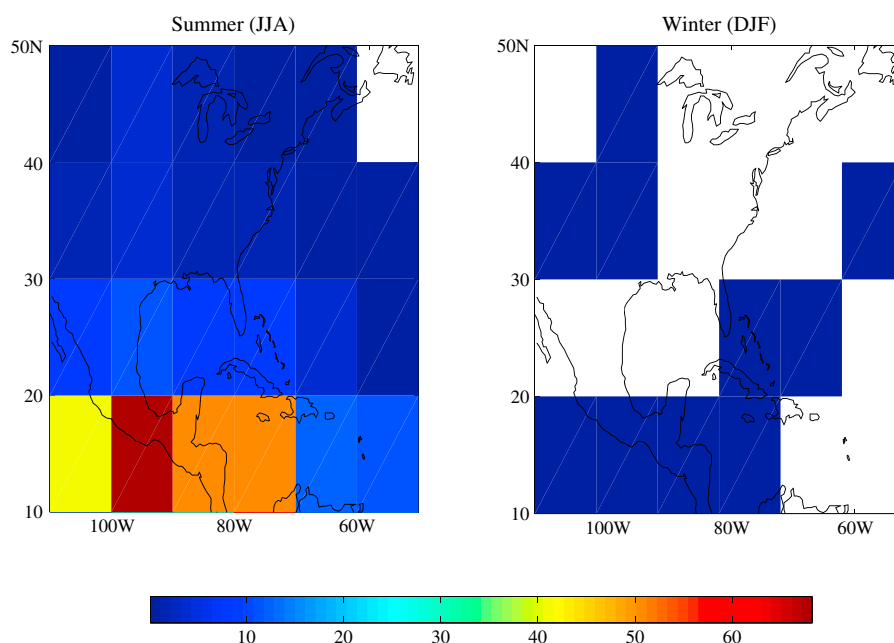
Figure 3. Climatology of DC frequency. Monthly counts of DC in each 10° × 10° box are denoted by different colors.

high-concentration samples are detected in the midlatitudes (30–50°N) (Figure 2c). High water vapor concentration samples are much scarcer at 380–390 K. Samples with concentration greater than 12 ppmv are mostly located in the North American midlatitudes (Figure 2b). The fact that few high-concentration SWV samples lie in the tropics agrees with the understanding that vertical transport of water vapor is subject to dehydration due to cold tropopause temperature within the tropics [*Holton and Gettelman*, 2001]. Separating the samples into different seasons (not shown), we find that most of the high-concentration samples (>8 ppmv) that are located above the 370 K isentropic surface and poleward to 30° latitude occur in summer. This well corresponds to the seasonality of DC activity to be discussed below.

We divide the study domain into 10° × 10° grid boxes. The frequency of DC documented in the ISCCP-CT data set of each grid box is shown in Figure 3 for both summer and winter. Most deep convections in the study domain happen in summer, while the occurrence rate in winter is much lower (zero in many midlatitude boxes). This is consistent with what is found in previous studies [e.g., *Laing and Fritsch*, 2007].

To examine how SWV changes with DC, the correlation coefficient is calculated in each 10° × 10° box between water vapor concentration and DC frequency. The correlation result at 100 hPa is shown in Figure 4. At this level, SWV is positively correlated with DC, suggesting that deep convection explains the seasonal variation of lower stratospheric water vapor. It is also noticed that water vapor concentrations at different vertical levels vary in an unsynchronized manner. At higher vertical levels water vapor concentration tends to be anticorrelated with DC. For example, in the 10–20° N band, the water vapor anomaly at 56 hPa is opposite to DC fluctuation. In the 30–40°N band, a phase lag between the 100 hPa SWV and DC can also be seen.

We note that the seasonality of DC and thus the correlation between DC and SWV are sensitive to the LBT threshold for DC identification. We find that if including shallower DC using a threshold temperature higher than or equal to 210 K, the number of DC in midlatitudes becomes higher in winter because winter cyclones frequently occur in this region. Considering that the high-concentration samples in the lower stratosphere occur predominantly in summer in the region (see Figure 2 and discussions above), this means it is necessary to use a low threshold value (195 K is used here) to screen out the shallow convections irrelevant to the problem investigated here.

3.2. Storm Versus Nonstorm Profiles

We examine the influence of DC on water vapor distribution by comparing composite vertical profiles of storm and nonstorm groups categorized based on the procedure explained in section 2. Since the
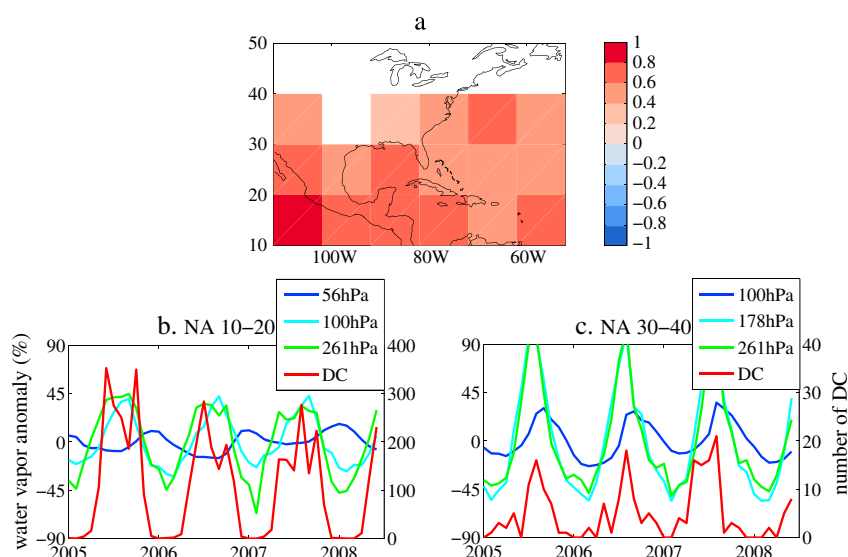
Figure 4. (a) Correlation between 100 hPa SWV and DC frequency in each $10° \times 10°$ box within the study domain. Only the correlation coefficients that pass 95% confidence level are shown. (b) Time series of SWV at a few selected levels and DC monthly count in the 10–20°N latitude band; (c) that in the 30–40° N band.

tropopause position at different latitudes is different, we divide the North American region (10–50°N, 50–112°W) into four 10° latitude bands. We calculate seasonal tropopause position based on both MLS and ERA-Interim temperature profiles. Both results suggest that in the low latitudes (10–30°N) tropopause does not have much seasonal variation and it is around 100 hPa. However, seasonal tropopause variation cannot be neglected in the midlatitudes (30–50°N). The lapse rate tropopause calculated based on MLS temperature profile is at 147 hPa in boreal summer and at 215 hPa in boreal winter in the 30–40° N band and is at 178 hPa and 215 hPa, respectively, in the 40–50°N band. The results calculated from ERA data are similar. So we examine vertical water vapor profiles in the 30–40° N and 40–50°N bands in summer (June–August) and winter (December–February), respectively. Results are shown in Figure 5.

The impact of deep convection is very noticeable. For example, in the 10–20°N band, MLS data show significant increase in water vapor concentration in the UTLS region in the storm samples as compared to the nonstorm samples (Figures 5a and 5b). This moistening signal is evident from the comparisons of most latitude bands.

Another noticeable feature is a dehydration signal at higher levels in the stratosphere, i.e., statistically significant decrease of water vapor concentration, e.g., around 40–60 hPa in the 10–20°N band. This signal is also observed in the other latitude bands. Using averaging kernels [*Livesey et al.*, 2011] of MLS water vapor products, we find that moistening in adjacent moistened lower layers cannot fully explain the drying signal. This suggests that there may be physical reasons that account for the dehydration observed.

We also calculate the probability distribution function (PDF) of water vapor concentration at identified wetter (or drier) levels in different latitude bands. Figure 6 shows noticeable differences between the storm and nonstorm cases. The difference is especially noticeable in the low-latitude band, where concentration in the storm cases leans toward higher values than the nonstorm cases (Figures 6a and 6b). This is consistent with the results above that DC is strongly correlated with enhanced moisture in the UTLS.

The results are verified using ACE-FTS water vapor data (not shown). The moistening-drying pattern seen from ACE-FTS data agrees well with the MLS results in most cases except that the position of dry signal derived using ACE data is a bit higher than that derived using MLS data in the midlatitudes. This is likely due to the different vertical coordinates used in retrieval for the two satellites [*Hegglin et al.*, 2013].

3.3. Trajectory Analysis

As shown by *Schwartz et al.* [2013], most high-concentration lower stratospheric water vapor samples are concentrated in the North American and Asian monsoon regions. If these high-concentration samples are
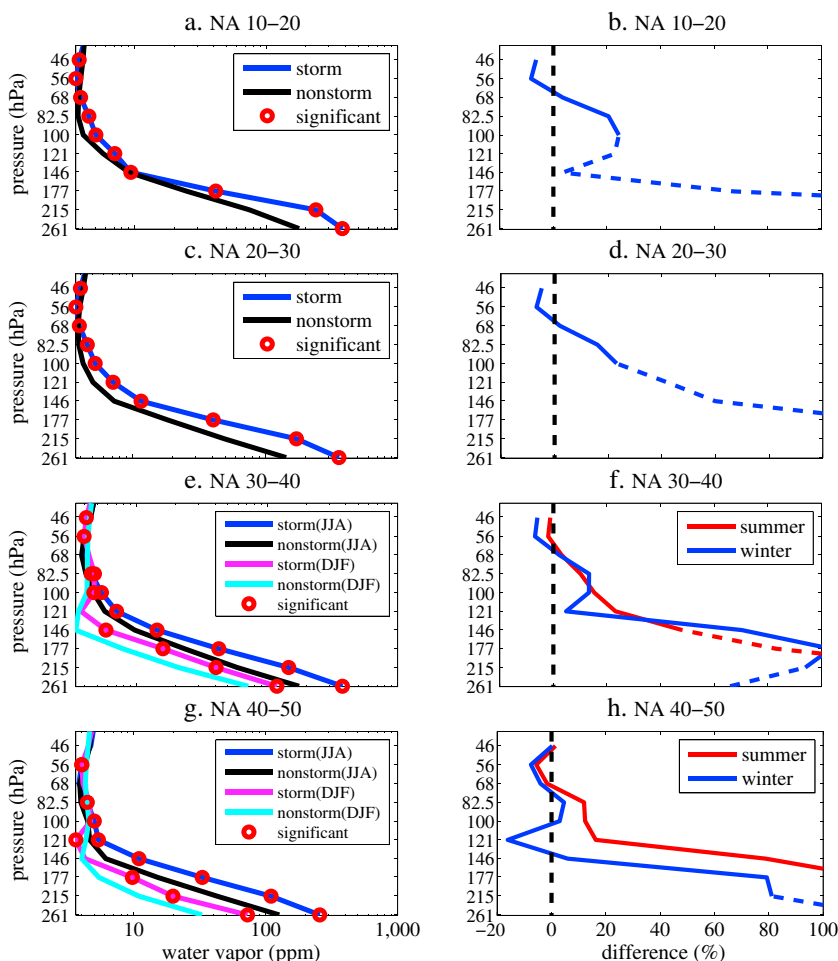
Figure 5. (a, c, e, and g) Composite water vapor profiles of the storm and nonstorm groups in four latitude bands are shown. MLS retrieval levels are labeled. The levels where the difference passes 95% confidence level (*t* test) are highlighted by red circles. (b, d, f, and h) Relative difference between the storm and nonstorm samples. Solid line represents the portion of the vertical profile that is above the seasonal mean tropopause height, and dashed line represents the portion below.

due to convective injection, it is expected that the samples are located within a reasonable time-space window around deep convection. Table 1 shows how the samples binned by their concentration values are divided into the storm and nonstorm groups. Interestingly, we find that a substantial fraction of the moist samples cannot be explained by collocated deep convection. For example, at 100 hPa half of the >8 ppmv samples (137 out of 166 samples) belong to the nonstorm group, almost double that in the storm group (13 out of 166). A possible explanation is long-range transport of high water vapor concentration air parcels. Here this effect is analyzed using the HYSPLIT trajectory model.

All samples with concentration greater than 8 ppmv in the North American region (10–50°N, 50–112°W) at 100 hPa are selected and set as the initial point to calculate back trajectories. With 20, 53, 47, and 17 samples in each latitude band, a total of 137 samples are examined in the trajectory analysis. Most of these samples are over the continent.

Since parcel release position influences trajectory result and there is uncertainty in the position of MLS samples (mainly due to its low vertical resolution), we calculate trajectories at multiple vertical levels (16, 16.5, 17, 17.5, and 18 km) around the level (100 hPa) where each sample is reported. As discussed in section 2, parcels are traced back at 48 h intervals up to 10 days. CSs that happened during the period are searched to determine whether each sample encountered DC. Here we define the influence region of one CS by the radius of each CS documented in the ISCCP data set. To simplify the procedure, 100 km is approximated as 1°. The search domain is enlarged by 1° in addition to account for the uncertainty in
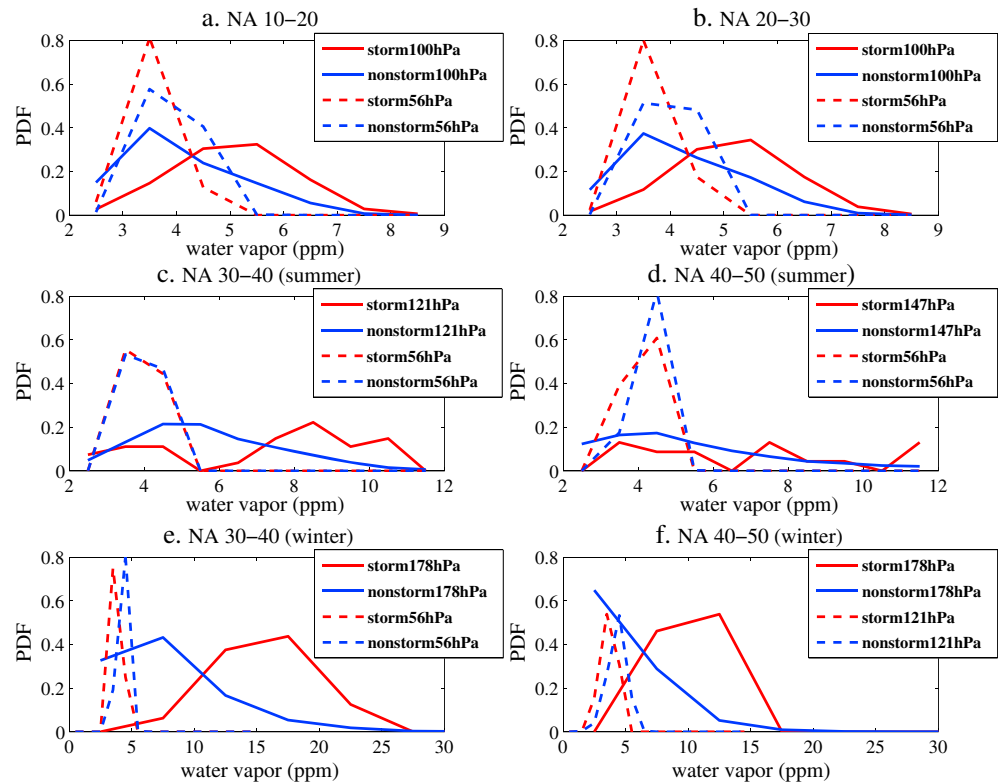
Figure 6. PDF of SWV at selected levels in each latitude band.

the CS influence region. If the trajectory crosses any CS influenced region, the high-concentration sample is tagged as "explained" by DC. For example, on 7 August 2005 8:00:00 UTC a high-concentration sample is detected at (17.8°N, 97°W). We trace back from this position and analyze back trajectories in five 48 h segments. As shown in Figure 7, the hourly positions of the parcel are recorded and the CSs that happened during the time are marked. In this case, two CS locations at 19°N that happened 45 h ago and two CS locations at 17°N that happened 20 h ago are found. This high-concentration sample will be regarded as being explained by DC within 20 h in history.

Following this procedure, each sample in the four latitude bands is traced back to search for DC encounters. Results derived using NCEP/NCAR reanalysis data are summarized in Figure 8. In the 10–20° N band, the tracking process is stopped at 8 days when there are no samples whose trajectory remains inside the domain with no DC encountered. Trajectory results explain 12 of the 20 samples in this band (Figure 8a). In comparison, 18/53 in the 20–30°N band, 26/47 in the 30–40°N band, and 11/17 in

Table 1. Number of Samples of Storm and Nonstorm Groups Falling Into Different Concentration Bins at Different Latitudes

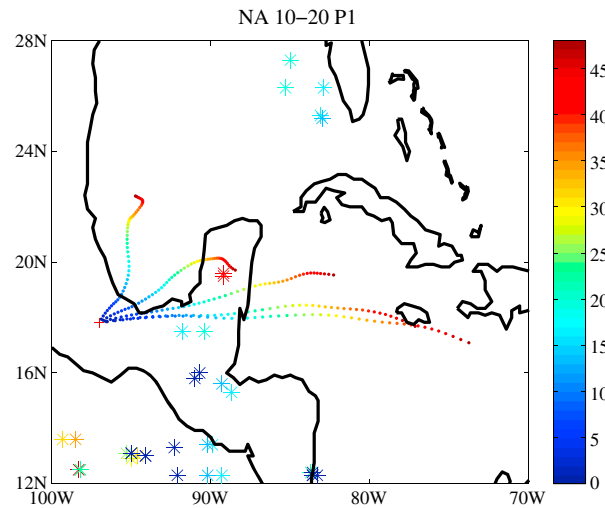| Latitude Band	Group	<2	2–3	3–4	4–5	5–6	6–7	7–8	>8
10–20°N	Storm	0	32	174	362	386	193	34	8
	Nonstorm	133	5,291	14,074	8,449	5,170	1,962	258	20
20–30°N	Storm	0	7	49	126	144	73	16	3
	Nonstorm	110	4,662	15,023	10,565	6,924	2,465	376	53
30–40°N	Storm	0	1	23	35	28	15	2	2
	Nonstorm	27	1,557	12,973	14,818	7,715	1,859	293	47
40–50°N	Storm	0	0	20	46	16	3	1	0
	Nonstorm	0	272	8,386	22,475	7,674	758	76	17

Figure 7. An illustration of the trajectory analysis. One high-concentration sample is observed at (17.8°N, 97°W) in August 2005 (marked by a red cross). From this initial position, the back trajectories in the first 48 h are shown here. The hourly positions are denoted by different colors. DCs that happened during the 48 h are color coded in the same way. Historical encounters with DC are determined by evaluating the distance between the sample position and DC location(s) at the same time.

the 40–50°N band are explained. In summary, only a fraction of these moist samples can be explained by DC; the unexplained samples amounts to 70, more than 40% of all the moist samples (a total of 166). Results derived using the EDAS data are similar.

Note that we have adopted a strict criterion (195 K threshold) for selecting DC and thus may have underestimated the likelihood of DC encountering. To examine this uncertainty, we relax the criterion to 245 K and re-search for DC along the trajectory. As a result, now more than 80% samples can be explained in the 10–20°N and 40–50°N bands. However, the ratio has little change in the 20–30°N and 30–40°N bands; there are still about 30% samples that cannot be explained. Furthermore, each sample is traced back at five vertical levels, and if any of these five trajectories encounters DC, the sample is categorized as explained. But despite all the reasons

that may have led to overestimation of DC encountering likelihood, a number of anomalously high concentration samples cannot be explained by either local vertical transport or long-range transport (up to 10 days and within the study domain).
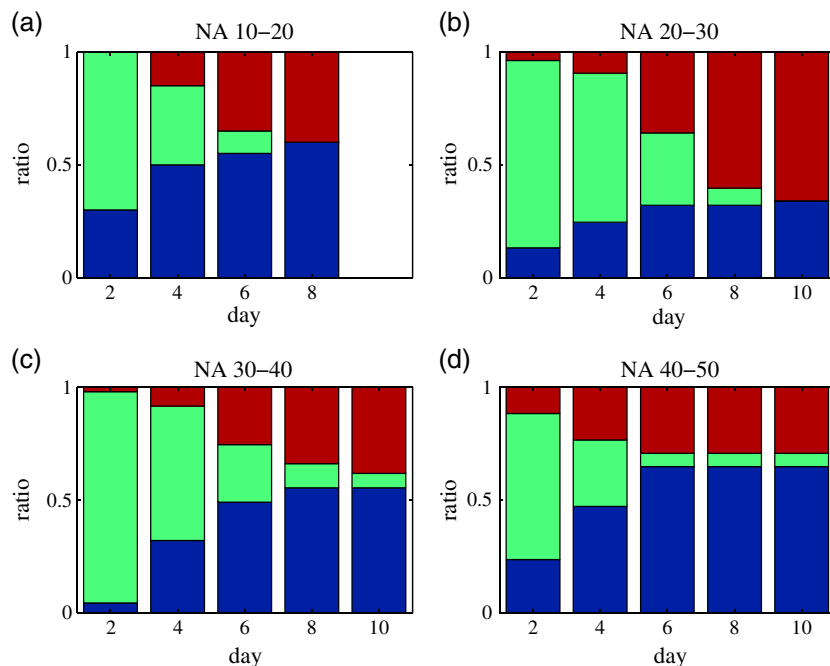

Figure 8. Ratio of high-concentration samples explained by DC. The horizontal axis shows the time of back tracking, and vertical axis is the ratio. Blue bars show the ratio of samples that are explained by DC. Red bars show that of samples whose trajectories extend outside the study domain without encountering any DC. Green bars show that of samples whose trajectories are still within the domain but without encountering any DC. The results are based on the trajectories derived from NCEP/NCAR reanalysis data.

4. Discussion and Conclusions

Using ISCCP convective tracking data to identify deep convection, we investigate the influence of deep convection on UTLS water vapor. We first compare MLS and ACE-FTS water vapor samples collocated with deep convection to those not collocated with deep convection. A typical pattern of a moistened UTLS layer overlaid by a drier upper layer is observed in both tropics and midlatitudes. We have also calculated the PDF of water vapor concentration at different UTLS levels, which corroborate the above results.

The drying signal above the moistened layer is interesting and was also identified by other studies [e.g., *Ray and Rosenlof*, 2007]. Our analysis based on the MLS weighting function suggests that this is not a spurious signal due to the vertical resolution of the retrieval data. The physical cause of this signal still eludes us and warrants further study.

It is found that many high-concentration water vapor samples cannot be explained by collocated deep convection. Using a back trajectory model, we investigate whether these samples can be caused by historical encounters with deep convection and long-range transport. Back trajectories are calculated by HYSPLIT model, using NCEP/NCAR and EDAS wind data. The attribution results derived from the two data sets are in good agreement. When tracked backward longer in time, more samples can be attributed to deep convection that happened along the trajectories. However, even when a relaxed criterion is used for determining the convective impact on the samples, a substantial fraction of samples, especially in the midlatitude bands, cannot be traced to any deep convection within the tracking domain (the North American region within the GOES-EAST field of view) and the time window (10 days). This may be due to small-scaled convection (radius less than 90 km) that is not observed by ISCCP data. Another plausible explanation is that these moist samples are due to longer-range (and time) transport. Pinning down the cause of these samples is beyond the scope of this paper but is an interesting topic for future work.

As discussed in the previous sections, DC identification (storm sample selection) is subject to the threshold LBT used in this study. A range of threshold values is tested. To minimize the impact of shallow (nonovershooting) convection on the storm composite, a rather low value of 195 K has been used for most of the results presented in this paper. On the other hand, the nonstorm composite is little impacted by this criterion owing to the much larger sample size. In general, the storm-nonstorm difference remains a moister UTLS layer overlaid by a drier layer, although the moistening in the lower stratosphere (at the MLS retrieval levels above the tropopause) becomes indiscernible in midlatitudes (30–40°N) when LBT threshold higher than 210 K is applied. In addition, we notice that the level that separates the drier upper layer from the moister lower layer goes upward when colder LBT threshold is used, which suggests that stronger overshooting deep convection "pushes" both moistened and dehydrated layers upward. Modeling results showed that high-capped DCs are more likely to moisten high stratosphere levels [*Dessler et al.*, 2007]. Our analysis provides observational evidence for this argument.

References

Anderson, J. G., D. M. Wilmouth, J. B. Smith, and D. S. Sayres (2012), UV dosage levels in summer: Increased risk of ozone loss from convectively injected water vapor, *Science*, *337*, 835–839, doi:10.1126/science.1222978.

Bedka, K. M., J. Brunner, R. Dworak, W. Feltz, J. Otkin, and T. Greenwald (2010), Objective satellite-based overshooting top detection using infrared window channel brightness temperature gradients, *J. Appl. Meteorol. Climatol.*, *49*, 181–202.

Bernath, P. F., et al. (2005), Atmospheric Chemistry Experiment (ACE): Mission overview, *Geophys. Res. Lett.*, *32*, L15S01, doi:10.1029/2005GL022386.

Brewer, A. W. (1949), Evidence for a world circulation provided by the measurements of helium and water vapor distribution in the stratosphere, *Q. J. R. Meteorol. Soc.*, *75*, 351–363, doi:10.1002/qj.49707532603.

Dee, D. P., et al. (2011), The ERA-Interim reanalysis: Configuration and performance of the data assimilation system, *Q. J. R. Meteorol. Soc.*, *137*, 553–597, doi:10.1002/qj.828.

Dessler, A. E., T. F. Hanisco, and S. Fueglistaler (2007), Effects of convective ice lofting on H_2O and HDO in the tropical tropopause layer, *J. Geophys. Res.*, *112*, D18309, doi:10.1029/2007JD008609.

Dessler, A. E., M. R. Schoeberl, T. Wang, S. M. Davis, and K. H. Rosenlof (2013), Stratospheric water vapor feedback, *Proc. Natl. Acad. Sci.*, *110*(45), 18,087–18,091.

Draxler, R. R., and G. D. Hess (1998), An overview of the HYSPLIT_4 modelling system of trajectories, dispersion, and deposition, *Aust. Meteorol. Mag.*, *47*, 295–308.

Forster, P. M. D., and K. P. Shine (1999), Stratospheric water vapour changes as a possible contributor to observed stratospheric cooling, *Geophys. Res. Lett.*, *26*(21), 3309–3312.

Fu, R., Y. L. Hu, J. S. Wright, J. H. Jiang, R. E. Dickson, M. X. Chen, M. Filipiak, W. G. Read, J. W. Waters, and D. L. Wu (2006), Short circuit of water vapor and polluted air to the global stratosphere by convective transport over the Tibetan Plateau, *Proc. Natl. Acad. Sci. U.S.A.*, *103*(15), 5664–5669, doi:10.1073/pnas.0601584103.

Fueglistaler, S., Y. S. Liu, T. J. Flannaghan, F. Ploeger, and P. H. Haynes (2014), Departure from Clausius-Clapeyron scaling of water entering the stratosphere in response to changes in tropical upwelling, *J. Geophys. Res. Atmos.*, *119*, 1962–1972, doi:10.1002/2013JD020772.

Hanisco, T. F., et al. (2007), Observations of deep convective influence on stratosphere water vapor and its isotopic composition, *Geophys. Res. Lett.*, *34*, L04814, doi:10.1029/2006GL027899.

Hartmann, D. L., et al. (2013), Observations: Atmosphere and surface, in *Climate Change 2013: The Physical Science Basis. Contribution of Working Group I to the Fifth Assessment Report of the Intergovernmental Panel on Climate Change*, edited by T. F. Stocker et al., pp. 159–254, Cambridge Univ. Press, U. K., and New York, doi:10.1017/CBO9781107415324.008.

Hegglin, M. I., et al. (2013), SPARC data initiative: Comparison of water vapor climatologies from international satellite limb sounders, *J. Geophys. Res. Atmos.*, *118*, 11,824–11,846, doi:10.1002/jgrd.50752.

Hegglin, M. I., et al. (2014), Vertical structure of stratospheric water vapour trends derived from merged satellite data, *Nat. Geosci.*, *7*, 768–776, doi:10.1038/ngeo2236.

Holton, J. R., and A. Gettelman (2001), Horizontal transport and the dehydration of the stratosphere, *Geophys. Res. Lett.*, *28*, 2799–2802, doi:10.1029/2001GL013148.

Huang, Y. (2013), On the longwave climate feedback, *J. Clim.*, *26*, 7603–7610, doi:10.1175/JCLI-D-13-00025.1.

Jiang, J. H., et al. (2010), Five-year (2004–2009) observations of upper tropospheric water vapor and cloud ice from MLS and comparisons with GEOS-5 analyses, *J. Geophys. Res.*, *115*, D15103, doi:10.1029/2009JD013256.

Kalnay, E., et al. (2006), The NCEP/NCAR 40-year reanalysis project, *Bull. Am. Meteorol. Soc.*, *77*, 437–470, doi:10.1175/1520-0477(1996) 077<0437:TNYRP>2.0.CO;2.

Kubar, T. L., D. L. Hartman, and R. Wood (2007), Radiative and convective driving of tropical high clouds, *J. Clim.*, *20*, 5510–5526.

Laing, A. G., and J. M. Fritsch (2007), The global population of mesoscale convective complexes, *Q. J. R. Meteorol. Soc.*, *123*, 389–405, doi:10.1002/qj.49712353807.

Livesey, N. J., W. Van Snyder, W. G. Read, and P. A. Wagner (2006), Retrieval algorithms for the EOS Microwave Limb Sounder (MLS), *IEEE Trans. Geosci. Remote Sens.*, *44*, 1144–1155, doi:10.1002/jgrd.50800.

Livesey, N. J., et al. (2011), EOS MLS version 3.3 level 2 data quality and description document version 3.3x-1.0, JPL D-33509, Jet Propul. Lab., Pasadena, Calif.

Machado, L. A. T., and W. B. Rossow (1993), Structure characteristics and radiative properties of tropical cloud clusters, *Mon. Weather Rev.*, *121*, 3234–3260, doi:10.1175/1520-0493(1993)121<3234:SCARPO>2.0.CO;2.

Machado, L. A. T., W. B. Rossow, R. L. Guedes, and A. W. Walker (1998), Life cycle variations of mesoscale convective systems over the Americas, *Mon. Weather Rev.*, *126*, 1630–1654, doi:10.1175/1520-0493(1998)1262.0.CO;2.

Newman, P. A., J. C. Wilson, M. N. Ross, C. A. Brock, P. J. Sheridan, M. R. Schoeberl, L. R. Lait, T. P. Bui, M. Loewenstein, and J. R. Podolske (2001), Chance encounter with a stratospheric kerosene rocket plume from Russia over California, *Geophys. Res. Lett.*, *28*, 959–962, doi:10.1029/2000GL011972.

Randel, W. J., E. Moyer, M. Park, E. Jensen, P. Bernath, K. Walker, and C. Boone (2012), Global variations of HDO and HDO/H_2O ratios in the upper troposphere and lower stratosphere derived from ACE-FTS satellite measurements, *J. Geophys. Res.*, *117*, D06303, doi:10.1029/2011JD016632.

Ray, E. A., and K. H. Rosenlof (2007), Hydration of the upper troposphere by tropical cyclones, *J. Geophys. Res.*, *112*, D12311, doi:10.1029/2006JD008009.

Read, W. G., et al. (2007), Aura Microwave Limb Sounder upper tropospheric and lower stratospheric H_2O and relative humidity with respect to ice validation, *J. Geophys. Res.*, *112*, D24S35, doi:10.1029/2007JD008752.

Rossow, W. B., A. W. Walker, D. Beuschel, and M. Roiter (1996), International Satellite Cloud Climatology Project (ISCCP) description of new cloud datasets, WMO/TD – No. 737, 115 pp., World Climate Research Programme (ICSU and WMO), Geneva, February 1996.

Schwartz, M. J., W. G. Read, M. L. Santee, N. J. Livesey, L. Froidevaux, A. Lambert, and G. L. Manney (2013), Convectively injected water vapor in the North American summer lowermost stratosphere, *Geophys. Res. Lett.*, *40*, 2316–2321, doi:10.1002/grl.50421.

Solomon, S., K. Rosenlof, R. Portmann, J. Daniel, S. Davis, T. Sanford, and G.-K. Plattner (2010), Contributions of stratospheric water vapor to decadal changes in the rate of global warming, *Science*, *327*, 1219, doi:10.1126/science.1182488.

Strong, M., Z. D. Sharp, and D. S. Gutzler (2007), Diagnosing moisture transport using D/H ratios of water vapor, *Geophys. Res. Lett.*, *34*, L03404, doi:10.1029/2006GL028307.

Takahashi, H., and Z. J. Luo (2014), Characterizing tropical overshooting deep convection from joint analysis of CloudSat and geostationary satellite observations, *J. Geophys. Res. Atmos.*, *119*, 112–121, doi:10.1002/2013JD020972.

Weinstock, E. M., et al. (2009), Validation of the Harvard Lyman-α in situ water vapor instrument: Implications for the mechanisms that control stratospheric water vapor, *J. Geophys. Res.*, *114*, D23301, doi:10.1029/2009JD012427.

World Meteorological Organization (1957), Meteorology: A three-dimensional science—Second session of the commission for aerology, WMO Bulletin IV(4), 134–138, WMO, Geneva.

Yuan, T., and Z. Li (2009), General macro- and microphysical properties of deep convective clouds as observed by MODIS, *J. Clim.*, *23*, 3457–3473.

Zipser, E. J., D. J. Cecil, C. Liu, S. W. Nesbitt, and D. P. Yorty (2006), Where are the most intense thunderstorms on Earth?, *Bull. Am. Meteorol. Soc.*, *87*, 1057–1071.